



This article appeared in a journal published by Elsevier. The attached copy is furnished to the author for internal non-commercial research and education use, including for instruction at the authors institution and sharing with colleagues.

Other uses, including reproduction and distribution, or selling or licensing copies, or posting to personal, institutional or third party websites are prohibited.

In most cases authors are permitted to post their version of the article (e.g. in Word or Tex form) to their personal website or institutional repository. Authors requiring further information regarding Elsevier's archiving and manuscript policies are encouraged to visit:

<http://www.elsevier.com/copyright>



# On the formation and growth of intermetallic phases during interdiffusion between low-carbon steel and aluminum alloys

H. Springer<sup>a</sup>, A. Kostka<sup>a,\*</sup>, E.J. Payton<sup>b</sup>, D. Raabe<sup>a</sup>, A. Kaysser-Pyzalla<sup>b,c</sup>, G. Eggeler<sup>b</sup>

<sup>a</sup> Max-Planck-Institut für Eisenforschung GmbH, 40237 Düsseldorf, Germany

<sup>b</sup> Institut für Werkstoffe, Ruhr-Universität Bochum, 44801 Bochum, Germany

<sup>c</sup> Helmholtz-Zentrum für Materialien und Energie GmbH, 14109 Berlin, Germany

Received 17 May 2010; received in revised form 4 November 2010; accepted 7 November 2010

Available online 15 December 2010

## Abstract

The formation of intermetallic reaction layers was investigated for interdiffusion between a low-carbon steel and commercially pure aluminum (99.99%) and between a low-carbon steel and an aluminum–silicon alloy (Al–5 wt.% Si). Solid/solid, solid/semi-solid and solid/liquid diffusion couples were produced at both 600 and 675 °C. The total width of the reaction layer is governed mainly by the parabolic diffusion-controlled growth of the  $\eta$  phase ( $\text{Al}_5\text{Fe}_2$ ), which exhibits orientation-dependent growth kinetics. The addition of Si to Al, which is known to decelerate reaction layer growth in interdiffusion experiments with Al melts, was found to accelerate the reaction layer growth in solid/semi-solid interdiffusion experiments. This phenomenon is discussed in light of previous atomistic explanations and the apparent activation energy calculated for the growth of the  $\eta$  phase ( $\text{Al}_5\text{Fe}_2$ ).

© 2010 Acta Materialia Inc. Published by Elsevier Ltd. All rights reserved.

**Keywords:** Interdiffusion; Joining; Intermetallic phases; Aluminum; Steel

## 1. Introduction

Iron (Fe) and aluminum (Al) alloys rank among the most important engineering materials because they provide good properties at low material cost in many applications [1]. Fe is the primary constituent of steels, which are versatile in structural applications where good creep resistance, formability or high strength are required [2,3]; Al alloys can provide excellent value in applications where low density and/or good corrosion resistance are desired [4,5]. Dissimilar joints between Fe and Al alloys are of significant importance due to the ubiquity of these materials in engineering applications.

The ability to form dissimilar joints between Fe and Al alloys is attractive because such bonds offer design engineers flexibility in many situations. While there is the obvious case of improving the strength-to-weight ratio in

construction and transportation systems [6,7], there also exist many other situations in which a good bond between Fe and Al alloys is highly desirable, such that the differing material properties of Al and Fe/steel may be exploited. For example, such joints may simultaneously provide high thermal conductivity and high-temperature corrosion resistance in household applications [8] as well as in the chemical industry [9]. In addition, they are used in the smelting production of Al [10]. While the specific properties that define a “good” bond vary between applications, it is universally acknowledged that joining of Fe and Al alloys is hindered by the large difference in melting temperatures, the difference in mechanical properties, and because of the formation of brittle intermetallic phases.

The Al–Fe phase diagram [11,12] shows a high solubility of Fe for Al and three Al-rich intermetallic phases:  $\zeta$  ( $\text{Al}_2\text{Fe}$ ),  $\eta$  ( $\text{Al}_5\text{Fe}_2$ ) and  $\theta$  ( $\text{Al}_{13}\text{Fe}_4$ ). The Al-rich side of the diagram presents a eutectic reaction in which the Fe-containing Al melt decomposes into  $\theta$  phase ( $\text{Al}_{13}\text{Fe}_4$ ) and Al. When silicon (Si) is present in the alloy, it plays

\* Corresponding author.

E-mail address: [a.kostka@mpie.de](mailto:a.kostka@mpie.de) (A. Kostka).

an important role in reactions with steels. There exists a reasonable understanding of the intermetallic phases which form in the Al–Fe–Si ternary system [13,14], and 11 ternary intermetallic phases have been found, possessing relatively large and closely positioned homogeneity ranges. The ternary eutectic phase is  $\tau_6$  ( $\text{Al}_{4.5}\text{FeSi}$ ), which forms with Al and Si from the liquid phase at 573 °C.

The phases that are observed when dissimilar metals come into contact at elevated temperatures depend on three factors: (1) the chemical potentials, (2) the nucleation conditions at the beginning of the interdiffusion process, and (3) the mobilities of the constituent elements [15]. As a result of (2) and (3), not all phases which appear in the phase diagram necessarily form. Since brittle intermetallic phases can be detrimental to the properties of joints between Al and Fe formed in welding, brazing, soldering and coating procedures [16,17], a fundamental understanding of the nucleation and growth kinetics of these phases is desired for development of improved materials and processes.

The early seminal work of Heumann and Dittrich [18] established via X-ray diffraction (XRD) that the  $\eta$  phase ( $\text{Al}_5\text{Fe}_2$ ) is the dominant reaction product at the interface between Fe and liquid Al, and showed that the rate of  $\eta$  phase growth follows a parabolic form in the temperature range 715–944 °C. Other works have confirmed the parabolic kinetics of  $\eta$  phase [19–21], and have detected an additional thin layer of  $\theta$  phase ( $\text{Al}_{13}\text{Fe}_4$ ) by transmission electron microscopy (TEM)-based selected-area diffraction (SAD) [20–22].

Gebhardt and Obrowski [23] studied the reaction between Fe and Al melts with a focus on the effect of additional elements on the growth of the reaction layer. Taking dilatometric measurements, they observed that additions of 2.5 wt.% Si reduce the apparent thickness of the intermetallic reaction layer by nearly a factor of three [23]. Later it was shown that the effect of Si is even more pronounced [24,25] and this phenomenon has since been exploited industrially to reduce the size of the brittle intermetallic layer during hot dip aluminizing [26] and other joining applications [7]. The critical limit for intermetallic layers in Al/Fe joints concerning their mechanical properties has been found to be about 10  $\mu\text{m}$  [16].

In all solid-state joining processes [27,28] (which by definition occur below the melting temperature of Al), interdiffusion conditions typically result in significantly thinner reaction layers as compared to those which form during hot dip aluminizing. Naoi and Kajihara [29] investigated Al/Fe interdiffusion couples between 550 and 640 °C for reaction times of up to 120 h using scanning electron microscopy (SEM) and electron probe microanalysis to study the reaction products. Their results clearly show that the  $\eta$  phase ( $\text{Al}_5\text{Fe}_2$ ) layer exhibits parabolic growth behavior and they claimed that no other phases formed [29]. Kurakin [30] analyzed roll-bonded samples of Fe in contact with thin (18  $\mu\text{m}$ ) Al–Si alloy layers containing 1.2 wt.% Si. Kurakin [30] used TEM electron diffraction and XRD to study the reaction products that formed after 30 min at

temperatures ranging from 250 to 600 °C. Kurakin [30] reported the formation of  $\text{Al}_{12}\text{Fe}_3\text{Si}$  phase (a body-centered-cubic phase with a chemical composition similar to that of the  $\tau_5$  phase ( $\text{Al}_8\text{Fe}_2\text{Si}$ )),  $\theta$  phase ( $\text{Al}_{13}\text{Fe}_4$ ) and  $\eta$  phase ( $\text{Al}_5\text{Fe}_2$ ), and mentioned the presence of pores in the Al alloy close to  $\eta$  phase ( $\text{Al}_5\text{Fe}_2$ ) in accordance with the observations of Heumann and Dittrich [18], but provided no microstructural evidence to support this claim. The fact that pores form during interdiffusion on the side of the couple with higher diffusion rates is well-known as the Kirkendall effect [31]. Kurakin [30] provided no thickness data, but attributed the influence of Si additions to Al on reaction layer growth to impeded diffusion caused by formation of the  $\text{Al}_{12}\text{Fe}_3\text{Si}$  phase.

Most of the previous kinetic work on interdiffusion processes in the Al–Fe system was performed after Fe or steel had reacted with Al melts; there remains very limited experimental data on solid/solid interdiffusion processes. While the addition of Si to Al has been found to decelerate reaction layer growth in solid/liquid interdiffusion experiments, the mechanism controlling this phenomenon is still not completely understood [32–34]. Although there are some published studies utilizing advanced characterization techniques to provide new microstructural insight into the build up of dissimilar steel–Al joints [35], these techniques have not yet been fully exploited to identify the fundamental microstructural processes associated with interdiffusion reactions in the Al–Fe system.

## 2. Objective

The present study attempts to elicit the microstructural parameters which govern the reaction kinetics for intermetallic layer growth during interdiffusion between Al and low-carbon steel under different conditions—with a special focus on understanding the effects of Si on the interdiffusion process—by combining interdiffusion experiments with orientation imaging (OIM) with electron backscatter diffraction (EBSD) using SEM and analytical TEM characterization techniques. Diffusion couples in several different states are considered in direct comparison: solid/solid, solid/liquid and solid/semi-solid. Semi-solid processing of Al alloys, in which the alloy is in a two-phase “mushy zone” where one phase is liquid and the other is solid, has recently received significant attention in the literature for its potential for near-net shape processing [36,37]. The objective of the present work is to contribute to an increased understanding of the fundamental scientific aspects of interdiffusion between Al alloys and steels in each of these material states. The results represent a basis which should allow engineers to improve joining process technology.

## 3. Materials and methods

Solid/solid, solid/semi-solid and solid/liquid interdiffusion experiments were performed between steel and Al

alloys. All steel samples investigated in the present study were cut out from 2 mm thick sheets of a low-carbon steel (0.08 wt.% C, European grade DC04). This steel was selected for its widespread use, for example in automotive applications (where it is used because it has good formability). The steel samples used for the solid/solid and solid/semi-solid interdiffusion experiments were ground and polished by standard metallographic techniques. The steel samples for solid/liquid experiments had a zinc (Zn) dip-coating of  $140 \text{ g m}^{-2}$ , resulting in a thickness of about  $20 \text{ }\mu\text{m}$ . The Al alloys used were cast blocks of either high-purity Al99.99 or Al containing 5 wt.% Si (AlSi5).

### 3.1. Solid/solid and solid/semi-solid interdiffusion experiments

Steel samples of  $2 \times 5 \times 5 \text{ mm}^3$  and Al samples of  $5 \times 5 \times 5 \text{ mm}^3$  were prepared by spark erosion. Their  $5 \times 5 \text{ mm}^2$  contact surfaces were ground and polished to a  $1 \text{ }\mu\text{m}$  finish by standard metallographic techniques, then cleaned ultrasonically in a bath of ethanol and acetone. The specimens were then clamped together with a small lateral displacement of the order of 0.5 mm to facilitate the location of the original contact plane after the annealing experiments and to provide a reference frame for analyzing the diffusion results. The experiments were performed in a horizontal glass tube furnace at  $600 \pm 5 \text{ }^\circ\text{C}$ . Prior to annealing, the furnace was evacuated and back-filled with argon (Ar). Cooling was performed outside the furnace after the thermal exposures were complete. At  $600 \text{ }^\circ\text{C}$  the binary Al–Si phase diagram [38] shows a two-phase region for the Al–5 wt.% Si alloy, consisting of about 50 wt.% solid phase and 50 wt.% melt. The chemical compositions of the solid and liquid phases of the Al–Si alloy are 1 and 9 wt.% Si, respectively. Throughout the duration of the experiment the semi-solid material remains sufficiently viscous to stay intact. The specimens were annealed for 1, 2, 4, 8 and 16 h under an Ar pressure of 1300 mbar. After the experiments, metallographic cross-sections were prepared by grinding and polishing perpendicular to the contact plane to study the reaction layers. TEM specimens were prepared from regions of interest across the cross-sections using a focused ion beam (FIB) technique, such that the TEM foil normal laid perpendicular to the normal of the plane of polish.

### 3.2. Solid/liquid interdiffusion experiments

The solid/liquid experiments were performed as dip tests, where the Zn-coated steel specimens with dimensions of  $130 \times 35 \times 2 \text{ mm}^3$  were immersed into an Al melt at  $675 \pm 10 \text{ }^\circ\text{C}$  under an Ar atmosphere of 400 mbar. The Zn coating of the steel substrate was used to improve the wetting of Al to the surface of the substrate instead of a salt-flux-based procedure. The coating assists in bringing the reaction partners into contact without the

interference of oxygen, and dissolves quickly when the material is immersed in the molten Al bath. The small quantities of Zn compared to the volume of the Al melt are not expected to affect the results of the experiment. Prior to hot dipping, the specimens were cleaned in acetone and a thermocouple was attached. The specimens were held above the Al melt until they reached  $200 \text{ }^\circ\text{C}$  prior to immersion. Specimens reached the reaction temperature within approximately 10 s after immersion. Specimens were allowed to react for 30 s after they reached reaction temperature. After the reaction time had passed, the specimens were pulled out of the bath and cooled in air. Metallographic cross-sections were prepared to study the reaction layers by grinding and polishing perpendicular to the prior solid/liquid interface, in a manner similar to the solid/solid and solid/semi-solid interdiffusion couples.

### 3.3. Characterization techniques

Interdiffusion couples were investigated using optical microscopy, XRD, SEM, EBSD and TEM. Thicknesses of the reaction layers were measured using a Leica DM4000M optical microscope, which was equipped with an Image Access 9 image analysis system. Average values of reaction layer thicknesses were determined following the same procedures as used in Refs. [19,29]. The cross-sectional area of the reaction layer was measured over a distance of  $150 \text{ }\mu\text{m}$ . Dividing this area by the length of the baseline yielded the average thickness. A Seifert ID002 X-ray spectrometer was used for phase identification. SEM was performed using a JSM 6500F equipped with a field emission gun, an EDAX energy dispersive X-ray spectroscopy (EDS) system and a TSL EBSD system [39]. EBSD was used to study crystallographic directions and to identify reaction phases. TEM samples of about  $25 \times 25 \times 0.1 \text{ }\mu\text{m}^3$  were prepared from the cross-sections using a JEM 9320 FIB with a  $\text{Ga}^+$  ion accelerating voltage of 30 kV. TEM was performed using a JEOL 2200 FS operating at 200 kV for bright-field (BF) imaging and scanning transmission electron microscopy (STEM) imaging, SAD and EDS chemical analysis. SAD patterns were indexed with the aid of the software package DDView 2004 (version 3.03) and the Powder Diffraction File PDF-2 (release 2004), both published by ICDD. A high-angle annular dark field (HAADF) detector was used in STEM mode [40,41] to obtain images with a high atomic number contrast between phases.

The intermetallic phases from the Al–Fe, and especially the Al–Fe–Si, systems have been referred to by different designations in the literature. The notations used throughout this paper are summarized in Table 1, along with the nominal stoichiometry and crystal structure information for each phase identified in the present work. In all cases, the phases were identified according to the chemical and crystallographic information provided in the references given in Table 1.



Table 1

Summary of the most common symbols, nominal stoichiometry and crystal structure information of the intermetallic phases identified in the present work, based on the provided references.

Symbol	Composition (approx.)	Space group; lattice	References
$\beta$	AlFe	$Pm\bar{3}m$ (221); cubic	[42]
$\kappa$	AlFe <sub>3</sub> C	$Pm\bar{3}m$ (221), cubic	[43]
$\eta$	Al <sub>3</sub> Fe <sub>2</sub>	$Cmcm$ (63); orthorhombic	[44]
$\theta$	Al <sub>13</sub> Fe <sub>4</sub>	$C2/m$ (12); monoclinic	[46]
$\tau_1$	Al <sub>2</sub> Fe <sub>3</sub> Si <sub>3</sub>	$P\bar{1}$ (2), triclinic	[14,47]
$\tau_2$	Al <sub>3</sub> FeSi	Monoclinic <sup>a</sup>	[14,48]
$\tau_3$	Al <sub>2</sub> FeSi	$Cmma$ (67); orthorhombic	[14,49]
$\tau_5$	Al <sub>8</sub> Fe <sub>2</sub> Si	$P6_3/mmc$ (194); hexagonal	[14,50]
$\tau_6$	Al <sub>4.5</sub> FeSi	$A2/a$ (15); monoclinic	[14,51]
$\tau_{10}$	Al <sub>4</sub> Fe <sub>1.7</sub> Si	$P6_3/mmc$ (194); hexagonal	[14,52]

<sup>a</sup> A discrepancy in the literature exists for the exact space group of this phase; however, the crystal system is uniformly reported as monoclinic.

## 4. Results

### 4.1. Interdiffusion between steel and solid Al at 600 °C

The results from the solid/solid interdiffusion experiments are given in Figs. 1–3. Fig. 1a and b compare SEM micrographs of reaction zones after 1 and 16 h of interdiffusion. It can be seen that the average thickness of the reaction layer increases from 5 to 36  $\mu\text{m}$  between the 1 and 16 h samples. Note that Fig. 1a and b are displayed at different magnifications. The reaction layers are continuous but their thicknesses vary along the baseline. The interface between the reaction layer and Al is serrated on a fine scale and the well-known [18,20,21,23,24,45] larger-scale wavy features are clearly visible on the steel side of the interface. Fig. 1a shows two types of reaction layers, which differ in gray level. Fig. 1c shows the area of the white sampling field in Fig. 1b at higher magnification. The thickness of the layer in contact with steel decreases from 1.5  $\mu\text{m}$  after 1 h to 0.2  $\mu\text{m}$  after 16 h, as can be seen by comparison of Fig. 1a with Fig. 1c. Fig. 1c also reveals dark features around 1  $\mu\text{m}$  in size. As annealing time increases, the number density of these dark features also increases.

Fig. 2 compiles representative results obtained from EBSD and EDX measurements for this sample condition. Fig. 2a shows an EBSD phase mapping result merged with EBSD image-quality data (in grayscale) obtained for the 1 h experiment. Fig. 2a clearly shows that the  $\eta$  phase (yellow) accounts for the majority of the reaction layer. Al and steel appear in green (Al) and red, respectively. Fig. 2b shows a SEM micrograph of the reaction layers after 8 h reaction time. The chemical composition of the reaction layer measured by EDX along the line indicated by the red arrow in Fig. 2b is shown in Fig. 2c. Complementary to the EBSD results, the Al concentration of 73 at.% corresponds to the  $\eta$  phase as the dominant component. The thin layers near the interface with the steel were identified by automated EBSD to have similar crystal structures as

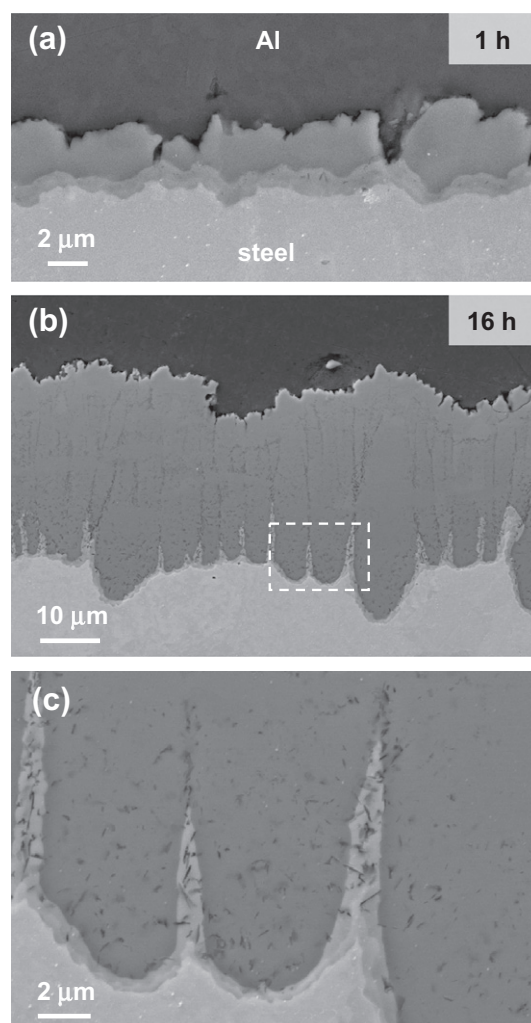


Fig. 1. SEM micrographs of the reaction zone between steel and Al99.99 after solid/solid interdiffusion at 600 °C: (a) after 1 h; (b) after 16 h. (c) Micrograph showing the area marked by the white rectangle in (b) at higher magnification.

steel and Al, respectively, and are thus colored red and green in Fig. 2a. To further investigate these thin layers at the transition zone near the steel, TEM samples were prepared from this area.

Fig. 3a shows a HAADF-STEM micrograph of the interfacial region between steel and the  $\eta$  phase after 16 h of interdiffusion. The dark area in the upper part of the figure represents a region of  $\eta$  phase; the corresponding electron diffraction pattern is given in Fig. 3b. The light gray area in the lower part of the micrograph represents steel. In Fig. 3a, two thin regions of slightly different contrast can be observed between  $\eta$  phase and steel, indicating a difference between either the crystal structure, the composition, or both. In the lower left part of the figure, the corresponding interfaces have been highlighted by white dashed lines. These thin layers were identified as  $\beta'$  phase and  $\kappa$  phase by SAD; corresponding patterns are shown in Fig. 3c and d, respectively. Diffraction data was complimented with EDX analysis, which yielded an Al

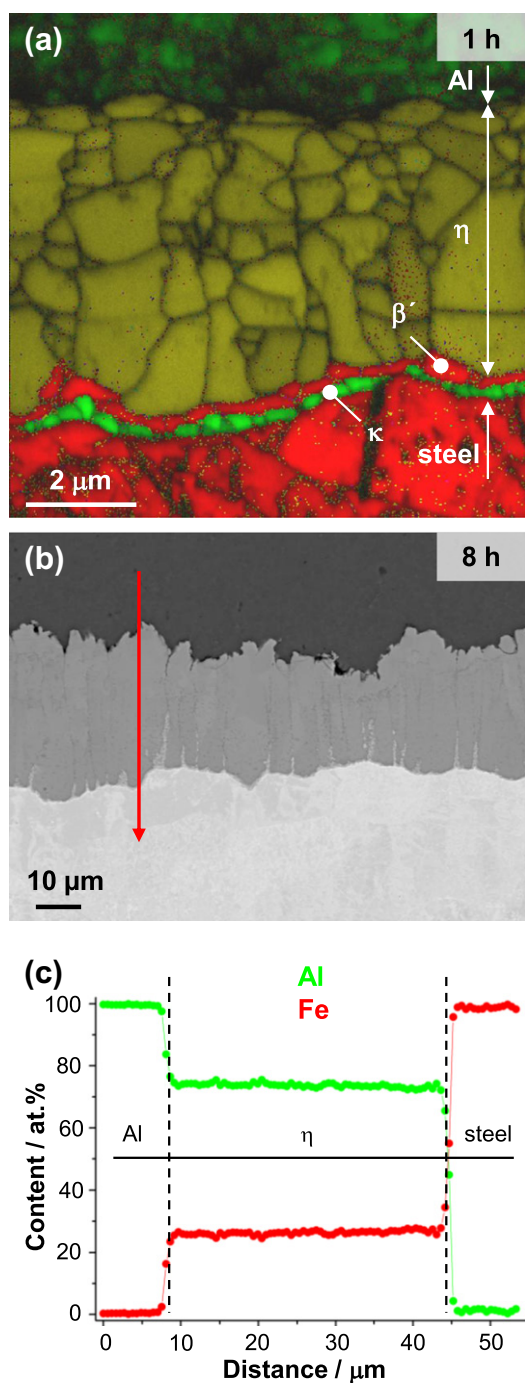


Fig. 2. Examples for SEM analysis of the reaction layer formed between steel and Al99.99 during solid/solid interdiffusion at 600 °C. (a) Color-coded EBSD phase map of the reaction zone between steel and Al after solid/solid interdiffusion for 1 h at 600 °C. Al and κ phase ( $\text{AlFe}_3\text{C}$ ) are shown in green, η phase ( $\text{Al}_3\text{Fe}_2$ ) is shown in yellow, and the steel and β' phase ( $\text{AlFe}$ ) are shown in red. The layers of κ and β' were identified by automated EBSD to have similar crystal structures to Al and the steel, respectively. (b) Micrograph of the reaction zone after 8 h. (c) EDX line scan result obtained along the red arrow in (b).

concentration of 39 at.% for the β' phase region and 17 at.% for the κ phase region. Note that the dark features that appear in Fig. 1 can also be detected in TEM, as shown in Fig. 3a. These defects were identified as small

pores by the absence of superlattice reflections or superimposed patterns in SAD. The pores are observed in β' and on the inner phase boundary of η grains close to the steel, but not in κ. The order of appearance and the specific phases that form in the reaction layers was not observed to depend on reaction time.

#### 4.2. Interdiffusion between steel and semi-solid Al–Si at 600 °C

Fig. 4 shows SEM micrographs taken after 1, 4 and 16 h of interdiffusion. The average total thickness of the reaction layer increases from 70 μm after 1 h to 288 μm after 16 h. Fine-scale features in the areas highlighted with white dashed rectangles in the left images are presented at higher magnifications in the right images, as indicated by the white arrows. The interface of the reaction layer towards the steel shows wavy features similar to those observed in the solid/solid interdiffusion experiments with Al (presented in Fig. 1). Adjacent to the Al–Si alloy, the interface of the reaction layer is also of an irregular shape. After 16 h, the reaction layer immediately adjacent to the Al–Si alloy is observed to have a thickness close to 50 μm, as shown in the left image of Fig. 4c. Between the layer adjacent to the Al–Si alloy and the layer adjacent to the steel, a smaller intermediate layer forms, with an approximate thickness of 40 μm, as can be seen in the right image of Fig. 4c. The reaction layer adjacent to the steel is 200 μm thick. In the high-magnification inserts of Fig. 4a and c, which correspond to 1 and 16 h reaction times, respectively, the boundaries between the three regions are highlighted by white dashed lines. With increasing annealing time, a growing number of pores can be observed in the middle reaction layer, on the side of the layer that is adjacent to the lower reaction layer in the images (which is itself adjacent to the steel). Additionally, an increasing number of small white particles appear in the layer adjacent to the steel, near the interface with the middle reaction layer, as can be seen by comparison of Fig. 4a and c. The high-magnification insert on the right side of Fig. 4b shows the interface between the steel and its adjacent reaction layer, which appears to have a similar constitution as the corresponding interface region in the solid/solid diffusion experiments shown in Fig. 1c. In the solid/semi-solid case, this layer is much thinner than in the solid/solid case, and does not extend continuously across the entire interface.

Fig. 5 compiles representative results obtained from EBSD and EDX measurements for this sample. Fig. 5a shows EBSD data for the 16 h experiment, corresponding to the sample shown in Fig. 4c. The result is reported as a color-coded phase map merged with the image-quality data in grayscale. The reaction layer adjacent to the steel consists of the η phase (yellow); the layer adjacent to the Al–Si alloy consists of the ternary eutectic phase  $\tau_6$  (violet). The color-coded map for the intermediate layer suggests the presence of very fine grains of different phases that could not be reliably identified by automated EBSD.

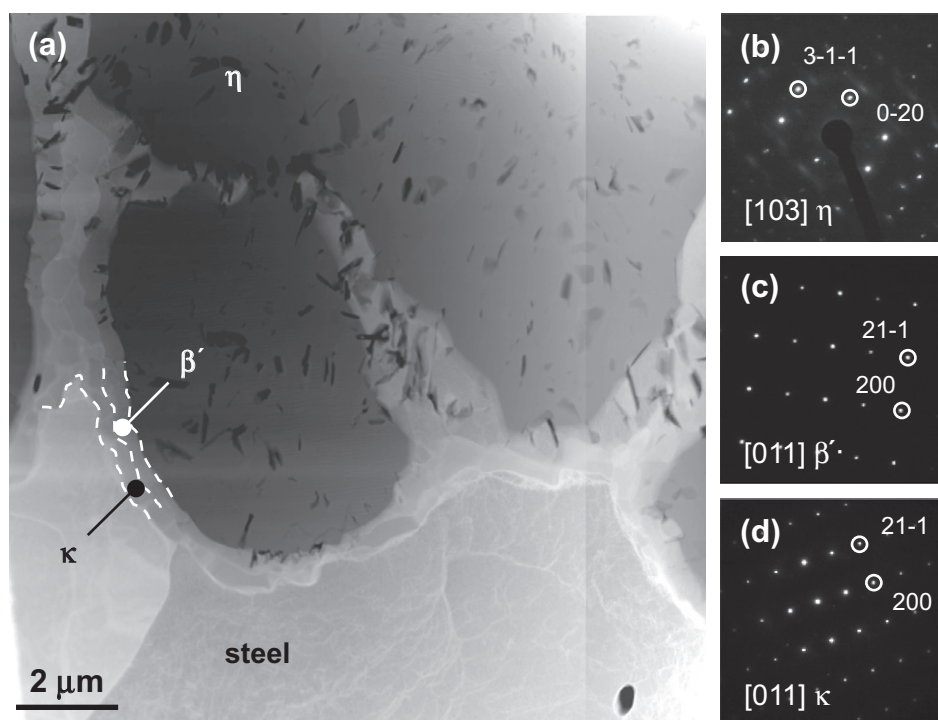


Fig. 3. TEM analysis of the interfacial region between steel and the  $\eta$  phase ( $\text{Al}_3\text{Fe}_2$ ) after 16 h solid/solid interdiffusion with Al99.99 at 600 °C: (a) STEM (HAADF) micrograph. (b–d) Characteristic SAD patterns taken from single-phase regions of  $\eta$ ,  $\beta'$  and  $\kappa$ , respectively. (For interpretation of the references to color in this figure legend, the reader is referred to the web version of this article.)

Fig. 5b shows a SEM micrograph of the reaction layers after 2 h reaction time. A red arrow indicates the position of a reference line along which chemical compositions were measured by EDX. The corresponding results are presented in Fig. 5c. The chemical composition of the reaction layer adjacent to the Al corresponds to the  $\tau_6$  phase, whereas the result for the reaction layer adjacent to the steel suggests the presence of  $\eta$  phase with small amounts of Si in solid solution (1–2 at.%). While the chemical compositions of the layers adjacent to the steel and Al are homogeneous and support the EBSD results, the intermediate layer shows strong local variations in composition. Additionally, the SEM pictures (Fig. 4) and the EBSD diagram (Fig. 5a) reveal fine-scale features in the intermediate layer and in the  $\eta$  phase layer adjacent to it.

In order to better interpret the SEM data, and to better characterize the multi-phase intermediate layer, TEM specimens were prepared from localized regions of the reaction layer by FIB extraction after 16 h annealing time, as shown in Fig. 6. Fig. 6a is a STEM HAADF micrograph from a transition zone that extends from the intermediate layer (at the top of the micrograph) to the  $\eta$  phase layer (at the bottom of the micrograph). The white marker in the inset SEM image indicates the location from which the TEM foil was extracted. The TEM micrograph clearly shows that there is Kirkendall porosity (with pores averaging approximately 1  $\mu\text{m}$  in diameter) in the intermediate layer and at the interface between the intermediate layer and the  $\eta$  phase layer. Typical electron diffraction patterns of phases found in the TEM foil shown in Fig. 6a are

presented in Fig. 6b–d. Three phases can clearly be differentiated:  $\tau_1$ ,  $\tau_3$  and  $\eta$ . The small white features observed in the  $\eta$  phase layer in Fig. 4a and c were identified as particles of the  $\tau_1$  phase.

Table 2 summarizes all information on the chemical (as measured by SEM-based EDX) and crystallographic nature (as characterized by TEM-based EBSD, XRD and SAD) of the phases that were detected in the solid/semi-solid interdiffusion experiments. Independent of the annealing time, the layer adjacent to the Al–Si alloy always consisted of the  $\tau_6$  phase and the layer adjacent to the steel was always the  $\eta$  phase, in which dispersed particles of the  $\tau_1$  phase appeared adjacent to the intermediate layer. These Si-rich particles appear to have precipitated within the  $\eta$  phase, as  $\eta$  contains only 1–2 at.% Si. The intermediate layer has a more complicated and time-dependent microstructure; up to four phases were found and the different phases consisted either of bands of greatly varying thickness or regions in which the phases were dispersed within one another.

#### 4.3. Interdiffusion between steel and liquid Al, steel and liquid Al–Si at 675 °C

Fig. 7–9 show the results of experiments performed to study the reaction layers which develop after 30 s. Fig. 7 presents the results for Al, while the results for Al–5 wt.% Si are given in Figs. 8 and 9.

Fig. 7a shows the well-known interfacial morphology after the reaction of either Fe or low-alloyed steel with



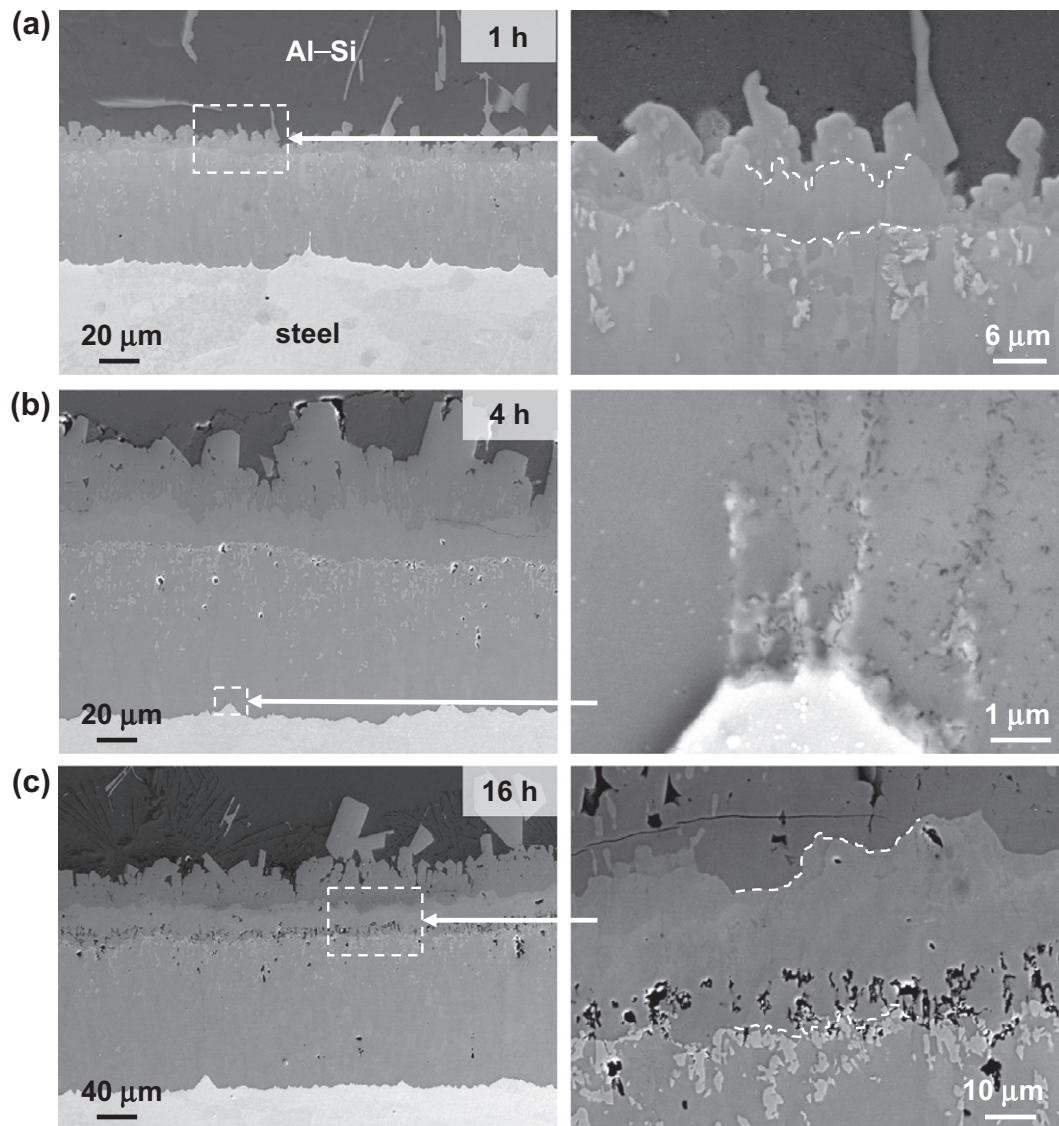


Fig. 4. SEM micrographs of the reaction zone formed between steel and Al–5 wt.% Si during solid/semi-solid interdiffusion at 600 °C: (a) after 1 h; (b) after 4 h; (c) after 16 h. Micrographs on the right are higher-magnification views of the areas in the left images that are marked by white rectangles.

liquid Al [18,20,21,23,24,45]. There is no flat interface between the intermetallic layer and the steel. Instead, tongue-like protrusions of the reaction layer into the steel base material are observed. No additional thin layers were observed directly adjacent to the steel, as were observed in the solid/solid and solid/semi-solid experiments presented in Figs. 1c and 4b. The interface between the reaction zone and the liquid Al is also irregular, but on a much finer scale.

Such protrusions as are observed in Fig. 7a for the interdiffusion between steel and liquid Al do not form during the reaction with the Si-containing melt, as can be seen in Fig. 8b. The interface between steel and the reaction layer is not tongue-shaped but flat, and toward the solidified Al–Si coating the interface is fringed with a few blocky excrescences. Comparison of Fig. 7b with Fig. 8c shows that adding Si to Al melts strongly reduces the thickness of the intermetallic layer during solid/liquid interdiffusion,

in agreement with findings frequently reported in the literature [23–26,32–34]. While the total thickness of the alloy layer is 36 μm for the reaction of steel with Al, it reaches only approximately 10 μm when 5 wt.% Si is added to the Al melt.

The EDX line scan result in Fig. 7b and the color-coded EBSD phase map of Fig. 7c show that the reaction layer that forms when the steel reacts with Al consists of two phases: an η phase layer adjacent to the steel (colored yellow in Fig. 7c) and a θ phase layer adjacent to the Al (colored blue in Fig. 7c). In contrast, three reaction layers can be differentiated when the steel reacts with the Si-containing melt, as can be seen in the line scan data of Fig. 8c, which was obtained along the red arrow in Fig. 8b. The chemical composition of the outer layer (in contact with the melt) matches that of the τ<sub>5</sub> phase. Two thinner layers follow: one with the same chemical composition as the θ phase and another that corresponds to the η phase. The θ phase



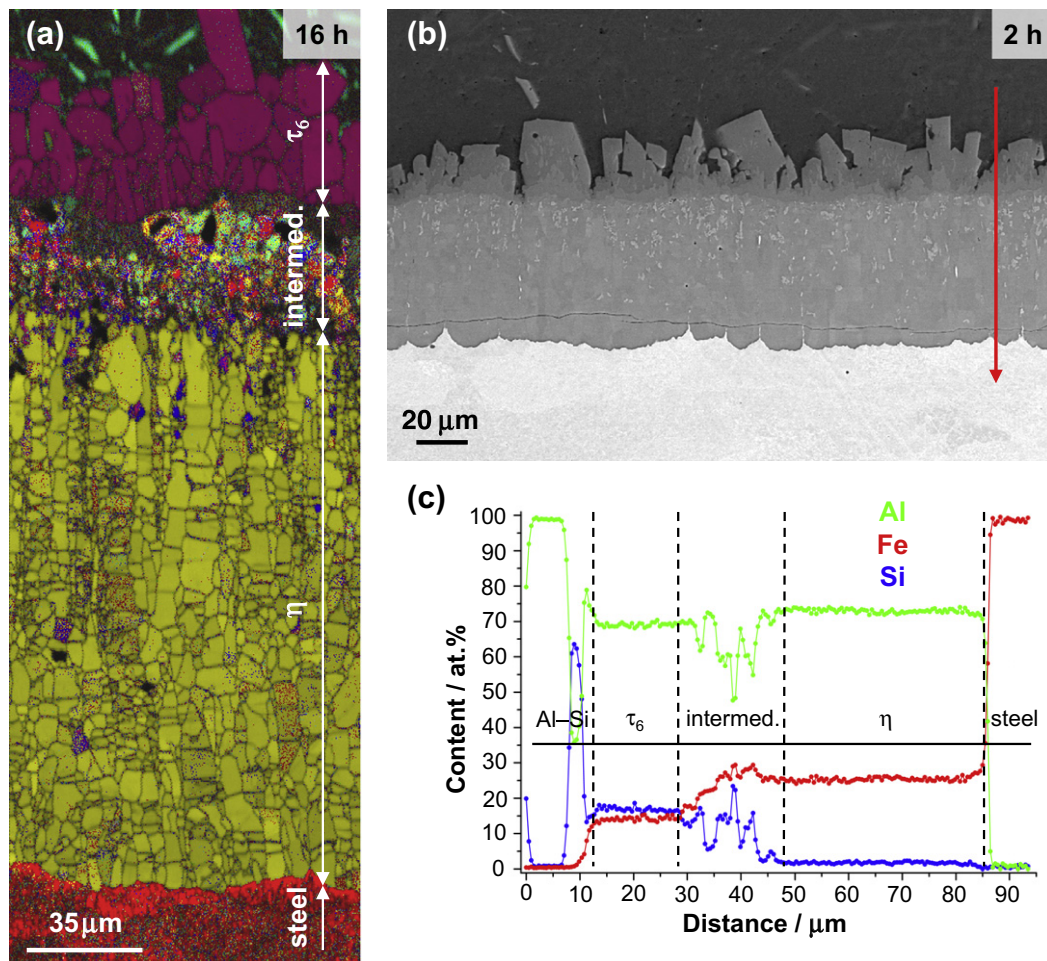


Fig. 5. Examples for SEM analysis of the reaction layer formed between steel and Al–5 wt.% Si during solid/semi-solid interdiffusion at 600 °C. (a) Color-coded EBSD phase map after 16 h (steel, red;  $\eta$  phase ( $\text{Al}_5\text{Fe}_2$ ), yellow;  $\tau_6$  phase ( $\text{Al}_{4.5}\text{FeSi}$ ), violet). (b) Micrograph of the reaction zone after 2 h. (c) EDX line scan result obtained along the red arrow in (b).

contains about 4–5 at.% Si in solid solution. The Si content of  $\eta$  phase, on the other hand, is lower and about the same as in the solid/semi-solid interdiffusion experiments that were shown in Fig. 5c, at around 1–2 at.%. While the thickness of the  $\theta$  phase layer remains constant, the thickness of the  $\eta$  layer changes irregularly across the sample, as shown in Fig. 8a.

Interestingly, the EDX results presented in Fig. 8c show a Si peak at the interface between  $\theta$  and  $\eta$ . To resolve the cause of the Si peak and confirm the EDX line scan results, TEM samples were prepared from a fringed section of the reaction layer using the FIB lift-out technique. A typical STEM HAADF micrograph of the reaction zone is shown in Fig. 9a. It should be noted that the solidified alloy at the top of the micrograph has a multiple-phase cast microstructure which was not investigated as part of the present work. Within the  $\tau_5$  phase, which was in direct contact with the melt and has the corresponding diffraction pattern of Fig. 9b, isolated “islands” of  $\theta$  phase can be found, such as the one marked with the downward-pointing white arrow in Fig. 9a. The black features, such as the one marked with the upward-pointing white arrow in Fig. 9a,

most probably represent pores. The  $\tau_5$  phase appears to be continuous along the reaction front (as “film-like” grains which are not clearly visible in Fig. 9). Moving toward the steel, a region can be observed that was identified via SAD as  $\theta$  phase, as shown in Fig. 9c. Between the  $\theta$  phase layer and the  $\eta$  phase layer (SAD pattern in Fig. 9d), a seam of isolated  $\tau_1$  particles (SAD pattern in Fig. 9e) can be seen in Fig. 9a, similar to the case of the solid/semi-solid interdiffusion experiments with an Al–Si alloy (Fig. 6). These  $\tau_1$  particles cause the Si peak in the EDX line scan result in Fig. 8c.

#### 4.4. Crystallographic comparisons of reaction layers from solid/solid, solid/semi-solid and solid/liquid interdiffusion

Fig. 10 presents inverse pole figure (IPF) EBSD maps merged with the grayscale image-quality data for two phases, the  $\eta$  phase and  $\tau_5$  phase, for the solid/solid, solid/semi-solid and solid/liquid diffusion experiments performed in this study. The results show the full reaction zones but the color-coded key only applies to the regions of orthorhombic and/or hexagonal symmetry—most

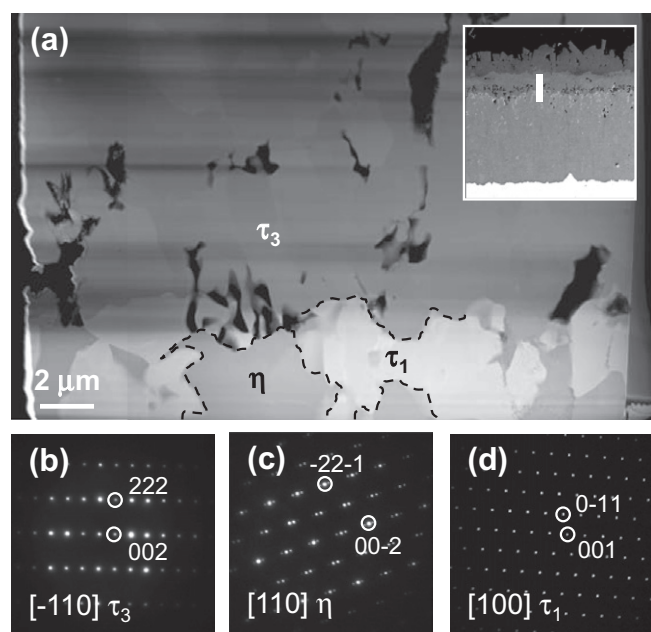


Fig. 6. TEM analysis of the interfacial region which forms between the  $\eta$  phase ( $\text{Al}_5\text{Fe}_2$ ) layer and the intermediate layer identified in Fig. 5a during the solid/semi-solid interdiffusion reaction between steel and Al–5 wt.% Si at 600 °C. (a) STEM (HAADF) micrograph with regions of key phases highlighted. The extraction location of the TEM foil is marked in the insert. (b–d) Characteristic SAD patterns taken from single-phase regions of  $\tau_3$ ,  $\eta$  and  $\tau_1$ , respectively.

importantly, regions of the  $\eta$  and  $\tau_5$  phases. These regions are marked by white double-sided arrows in all maps of Fig. 10. In all cases the locations of the Al alloy and the steel are on the top and on the bottom of the map, respectively. Fig. 10a shows the results obtained for the reaction zone which forms during the interdiffusion between the steel and the Al–Si melt. The IPF map in Fig. 10a suggests that only one crystallographic direction prevails in the  $\tau_5$  phase layer at the top of the region. Fig. 10b shows IPF results for the  $\eta$  phase that were obtained for the solid/liquid interdiffusion experiment between steel and the Al melt. In agreement with earlier findings [18], large columnar grains grow along the  $c$ -axis of the phase, as indicated by its appearance mostly in green and blue colors, showing that the grains are oriented normal to the  $c$ -axis. The dark horizontal lines of low image quality within the columnar regions of relatively uniform shades of color indicate the

presence of small-angle twist boundaries within the columnar grains. The IPF results for the solid-state reaction product that forms during the interdiffusion between steel and solid Al is shown in Fig. 10c. A comparison with Fig. 10b suggests that it does not matter whether the  $\eta$  phase forms as a result of a reaction between steel with liquid or solid Al. In both cases, large columnar grains are obtained, oriented perpendicular to the  $c$ -axis. Fig. 10c shows two maps, one for 1 h and another for 16 h reaction time at 600 °C. Short reaction times result in small  $\eta$  phase grains with different grain orientations, as shown in the upper map in Fig. 10c. After 16 h, large columnar grains oriented perpendicular to the  $c$ -axis are observed, as depicted in the lower map in Fig. 10c. The IPF presented in Fig. 10d shows  $\eta$  phase orientations in the layer which forms during interdiffusion between steel and the semi-solid Al–Si alloy. Similar to the case with the  $\eta$  layers in all other experimental results, the majority of the large columnar  $\eta$  phase grains are oriented perpendicular to the  $c$ -axis of the phase.

#### 4.5. Kinetics of the interdiffusion reaction in comparison to previously published values

The kinetics of reaction zone growth will now be considered. Fig. 11 shows results from the interdiffusion reaction between steel and Al. In Fig. 11a, the layer thicknesses (with  $d$  in  $\mu\text{m}$ ) are plotted as a function of square root of time (with  $t$  in h) after reaction at 600 °C. The two conditions shown in Fig. 1a and b are represented by empty circles, while all other experiments from the present study are displayed as solid filled circles. Two additional values are given in the case of the 16 h experiment: the maximum and minimum thickness of the layer, shown as error bars to indicate the experimental scatter associated with the data. The combined thickness values of the  $\beta'$  and  $\kappa$  layers are shown as solid filled squares. The good agreement of the data to a parabolic form,

$$d = k \cdot \sqrt{t}, \quad (1)$$

where  $k$  is a temperature-dependent rate constant, suggests that growth of the reaction layer is controlled by the diffusion of Al and/or Fe atoms through the  $\eta$  phase. The slope of the total thickness data shown in Fig. 11a produces a rate constant of  $0.185 \mu\text{m s}^{-1/2}$ .

Table 2

List of phases and their location in the reaction zone for the solid/semi-solid interdiffusion reaction between steel and Al–5 wt.% Si at 600 °C after different annealing times. The superscripts specify by which characterization method the respective phases were identified: (1) EDX in SEM; (2) EBSD; (3) SAD in TEM; (4) XRD.

Components	Al–5 wt.% Si				
	$\tau_6^{(1)(2)}$				
	$\theta^{(1)(2)} + \tau_3^{(1)} + \tau_5^{(1)(2)}$	$\theta^{(1)(2)} + \tau_3^{(1)} + \tau_5^{(1)(2)}$	$\theta^{(2)} + \tau_3^{(1)} + \tau_2^{(1)} + \tau_5^{(2)}$	$\tau_3^{(1)(4)} + \tau_2^{(4)} + \tau_{10}^{(1)(4)}$	$\tau_3^{(1)(3)(4)} + \tau_2^{(4)} + \tau_{10}^{(1)(4)}$
	$\eta^{(1)(2)(3)(4)} + \tau_1^{(1)(3)}$				
	Steel				
Time (h)	1	2	4	8	16

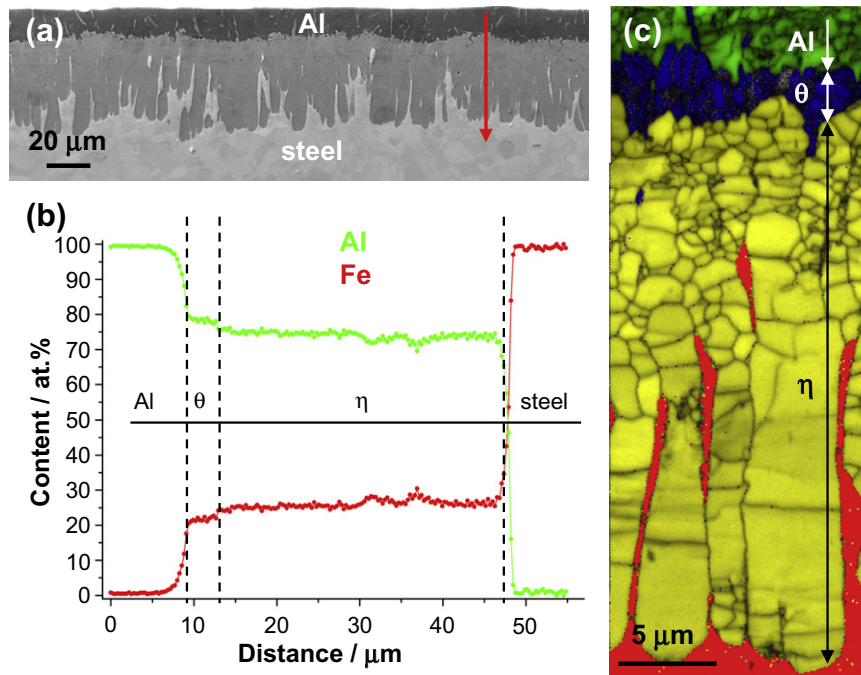


Fig. 7. SEM analysis of the reaction zone formed between steel and Al99.99 at 675 °C after 30 s (solid/liquid interdiffusion): (a) SEM micrograph. (b) EDX line scan result obtained along the red arrow in (a). (c) Color-coded EBSD phase map (Al, green;  $\eta$  phase ( $\text{Al}_5\text{Fe}_2$ ), yellow;  $\theta$  phase ( $\text{Al}_{13}\text{Fe}_4$ ), blue; steel, red).

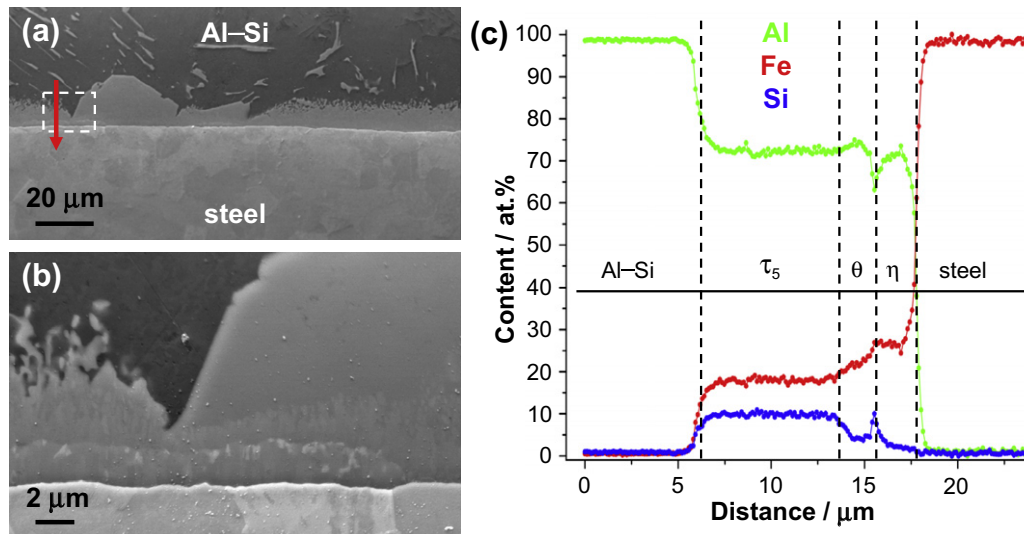


Fig. 8. SEM analysis of the reaction layer formed between steel and Al-5 wt.% Si during solid/liquid interdiffusion after 30 s at 675 °C. (a) Micrograph showing the two types of interface morphology of the reaction layer towards the solidified Al-Si coating. (b) Higher-magnification micrograph showing the area highlighted by the white rectangle in (a). (c) EDX line scan result obtained along the red arrow in (a).

Following the methodology of numerous other researchers [18–21,24,26,53], it was assumed that the solid/liquid reactions (Section 4.3) also followed a parabolic rate law. The thicknesses of the reaction layers were therefore plotted as function of square root of time (not shown here) to derive respective rate constants. Fig. 11b shows that the rate constants obtained from the data in Fig. 11a (displayed as an solid filled circle) as well as from the interdiffusion experiments with Al at 675 °C (displayed as a empty

circle) are in reasonable agreement with the results of other researchers [19,29,54].

Fig. 12 shows results from the interdiffusion reaction between steel and the Al-Si alloy. The thickness of the  $\tau_6$  layer, the inhomogenous intermediate layer and the  $\eta$  phase layer observed in the 600 °C case are plotted as a function of square root of time in Fig. 12a. While the  $\eta$  phase layer (displayed as solid filled circles) remains the dominant component and shows the fastest growth, the



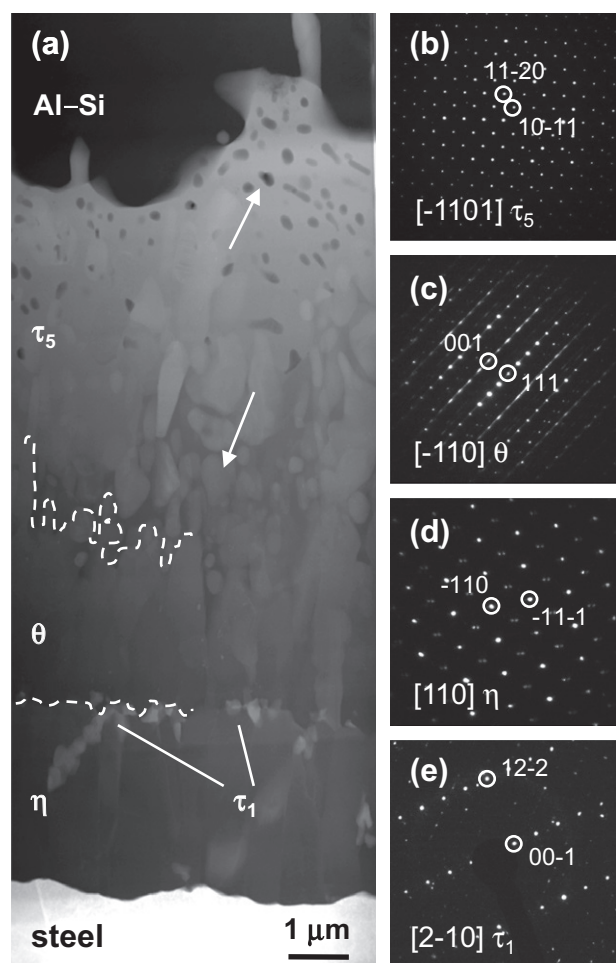


Fig. 9. TEM analysis of the reaction zone formed between steel and Al–5 wt.% Si during solid/liquid interdiffusion after 30 s at 675 °C. (a) STEM (HAADF) micrograph with regions of key phases highlighted. (b–d) Characteristic SAD diffraction patterns taken from single-phase regions of  $\tau_5$ ,  $\theta$ ,  $\eta$  and  $\tau_1$ , respectively.

other layers are observed to make a significant contribution to the overall reaction layer thickness (unlike in the experiments with unalloyed Al considered above).

Following the same procedure as described for Fig. 11b, the rate constants from the Al–Si alloy experiments were obtained from fits to parabolic rate laws. The results of this analysis are presented in Fig. 12b. Three rate constants are shown: the value derived from the data shown in Fig. 12a (600 °C interdiffusion; semi-filled circle); a rate constant obtained for 675 °C (empty circle); and a value which was evaluated from thickness data reported for 791 °C where a low-alloyed steel reacted with an Al melt with 2 wt.% Si [24] (empty square). In order to allow a comparison between the kinetic data for the two Al alloys (with and without Si), only the respective rate constants for the  $\eta$  phase are shown in Fig. 12b. This approach is in reasonable agreement with the microstructural data (Figs. 4 and 5 [24]); only in the case of the solid/liquid experiments with the Al–Si alloy does the  $\eta$  phase not take up the largest fraction of the reaction layer (Fig. 9).

Apparent activation energies ( $Q$  in  $\text{kJ mol}^{-1}$ ) can be determined from the results reported in Figs. 11b and 12b according to:

$$k = k_0 \cdot \exp\left(-\frac{Q}{R \cdot T}\right). \quad (2)$$

A value of  $190 \text{ kJ mol}^{-1}$  was found for the parabolic reaction layer growth (with  $\eta$  as the dominant component) for the reaction with pure Al, while  $17 \text{ kJ mol}^{-1}$  was obtained for the  $\eta$  phase growth in case of the reaction of steel with Al–Si alloys.

Fig. 13 presents optical micrographs which highlight one key result of the present study: Si is observed to have the opposite effect on the reaction layer thicknesses compared at different interaction temperatures. Fig. 13a and b show reaction layers which were obtained after 30 s solid/liquid interdiffusion between steel and Al and Al–5 wt.% Si, respectively. Here the well-known [23–26,32–34] growth reduction of reaction layers with Si-containing Al melts can be observed. Fig. 13c and d show reaction layers after 1 h interdiffusion at 600 °C between steel and Al and Al–5 wt.% Si, respectively. At this temperature, Si no longer impedes reaction layer growth; rather, it is observed to promote reaction layer growth.

## 5. Discussion

The  $\eta$  phase consistently makes up the largest fraction in the reaction layers that form during interdiffusion between low-carbon steel and either solid or liquid Al, and it is well-known that Si additions can be used to reduce the  $\eta$  layer growth rate when the Al–Si alloy is liquid. Heumann and Dittrich [18] concluded from their XRD data that the  $\eta$  phase grows preferentially along its  $c$ -axis (an observation corroborated by the EBSD results in Fig. 10 of the present work), and proposed that the rapid growth of the  $\eta$  phase along this crystallographic direction is facilitated by a highly open structural arrangement of atoms (“structural vacancies”). After it was shown that the enrichment of Fe in pure and Si-containing Al melts occurs at the same rate, it was concluded that Si affects the solid-state reaction rather than acting in the melt [24], and the matter has received little attention in the literature for some time. As a striking new result, we find that—opposite to what is observed at 675 °C—the thickness of the layer of  $\eta$  phase that forms during interdiffusion between steel and semi-solid Al–5 wt.% Si at 600 °C is significantly larger than when the steel is reacted with pure Al at the same temperature (Fig. 13). The fact that  $\eta$  phase growth is well described by a parabolic rate law in all cases makes it unlikely that interface reactions can account for this new finding.

This result casts into doubt earlier proposed atomistic explanations for the effect of Si on the growth of the  $\eta$  layer. Nicholls [32] proposed that Si may reduce the atomic mobility in the  $\eta$  phase by occupying the structural vacancies. If this were the case, one may expect a higher

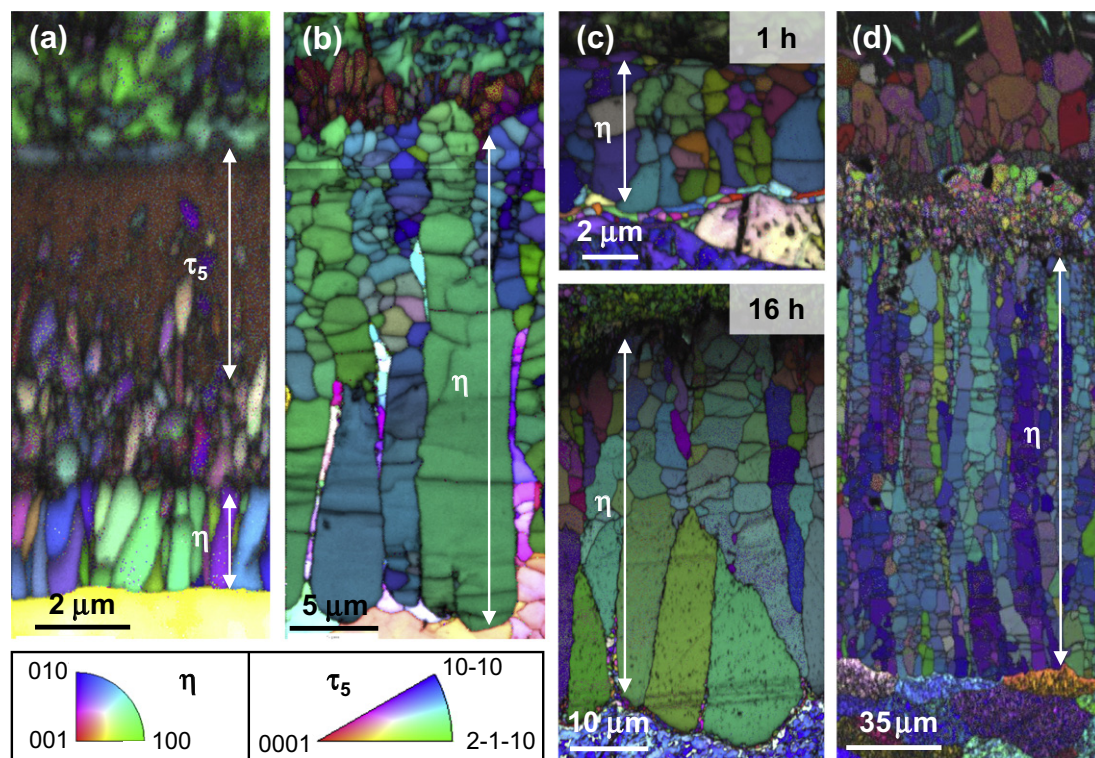


Fig. 10. EBSD inverse pole figure maps for different reaction layers between steel and Al alloys. Orientation triangles apply for  $\eta$  phase ( $\text{Al}_5\text{Fe}_2$ ) and  $\tau_5$  phase ( $\text{Al}_8\text{Fe}_2\text{Si}$ ) regions as marked by double white arrows. (a) Solid/liquid interdiffusion (675 °C, 30 s) with Al-5 wt.% Si. (b) Solid/liquid interdiffusion (675 °C, 30 s) with Al99.99. (c) Solid/solid interdiffusion (600 °C, 1 h (top) and 16 h (bottom)) with Al99.99. (d) Solid/semi-solid interdiffusion (600 °C, 16 h) with Al-5 wt.% Si.

concentration of Si in the  $\eta$  phase when its growth rate is reduced. The EDS results of the present study, however, suggest that the Si concentration of the  $\eta$  phase is roughly the same in the reactions with both the semi-solid and liquid Al-Si melts (1–2 at.%), though the growth rate of the  $\eta$  layer formed during interdiffusion with the Al-Si alloy at 600 °C is clearly significantly larger than that of the reaction with pure Al at the same temperature (Fig. 13c and d).

The faster growth of the  $\eta$  phase at lower temperatures is consistent with the Arrhenius plots in Figs. 11b and 12b: the lines of best fit give both a higher activation energy (slope) and a higher value of  $k_0$  (intercept) for the case of the unalloyed Al, resulting in the fit lines for the Si-containing alloy and for pure Al crossing one another. The intersection of the lines indicates that, at some temperature, the reaction layer will grow more quickly in the case of the Si-containing alloy than in the pure Al case. The fit lines in the present study place this critical temperature at around 668 °C, which happens to be close to the solidification temperature of unalloyed Al (~660 °C). It is worth noting again that the system at 600 °C consists of two phases, both of which have a volume fraction close to 50%: a solid phase with 1 wt.% Si and a liquid phase with 9 wt.% Si. Thus, it is difficult to draw clear conclusions to provide a new explanation of the exact mechanism responsible for the effect of Si from the present results because the line of best fit in Fig. 12b corresponds to only three data points, which have different Si contents:

2 wt.% at 791 °C [24], 5 wt.% at 675 °C, and 9 wt.% in the liquid phase at 600 °C. While further work is clearly required to further explain this phenomenon, in light of the present results it is difficult to maintain that structural vacancy obstruction by Si atoms is responsible for the reduction in growth rate.

The advanced microscopy techniques applied in the present work (such as site-specific TEM foil preparation with the FIB) were able to resolve and identify several new features in the reaction zones that, to the authors' knowledge, have not been previously reported. When steel reacts with a pure Al melt at 675 °C, a small layer of  $\theta$  phase is detected between the  $\eta$  and the Al (Fig. 7), in agreement with previous TEM work [22]; however, when the reaction occurs with solid Al at 600 °C, no  $\theta$  is detected and very thin layers of  $\beta'$  and  $\kappa$  phases can be identified between the  $\eta$  phase and the steel (Fig. 3). The TEM and EBSD results clearly indicate that there are different phases bordering the  $\eta$  phase in all of the present experiments. It cannot be ruled out that this difference may play a role in the observed effects of Si on the growth rate of the  $\eta$  layer during interdiffusion between steel and Al alloys.

The microstructure of the reaction layer after interdiffusion between steel and Al-5 wt.% Si at 600 °C (Fig. 5, Table 2) is much more complex than the respective layers formed between steel and pure Al (Figs. 2 and 3). The ternary phase  $\tau_6$  consistently takes up the outer part of the reaction layer (Table 2). The fact that the  $\tau_6$  phase layer

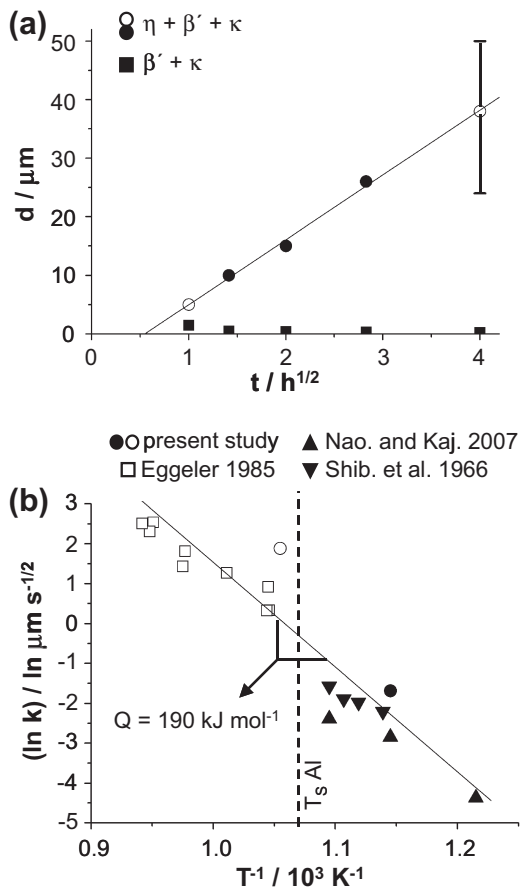


Fig. 11. Growth of the reaction layer during the reaction of steel with Al99.99. (a) Thickness data from the present study plotted as a function of the square root of reaction time at 600 °C. (b) Arrhenius plot of rate constants  $k$  in  $\mu\text{m s}^{-1/2}$  from the present study and from the literature [19,29,54].

grows as a function of time (Fig. 12a) suggests that this ternary eutectic phase forms mainly as a result of the interdiffusion process rather than during solidification. The presence of a heterogeneous intermediate layer between  $\tau_6$  and  $\eta$  (Figs. 5 and 6, Table 2), consisting of a mixture of coexisting binary Al–Fe and ternary Al–Fe–Si phases, seems reasonable when taking the ternary Al–Fe–Si phase diagram [13] into account. The results presented in Table 2 also illustrate an evolution in terms of the composition of this heterogeneous layer during the interdiffusion reaction. Only the  $\tau_3$  phase is detected in all cases. In contrast, the phases  $\theta$  and  $\tau_5$ , which are detected in early stages, disappear after 8 h reaction time, and new phases (such as  $\tau_{10}$  and  $\tau_2$ ) are formed. Additional work is required to determine whether the features of the fine-scale microstructure observed in the intermediate layer in Fig. 5a are solely related to the interdiffusion process or if cooling from 600 °C to room temperature also has an effect.

## 6. Summary and conclusions

The present study tracked the evolution of the reaction zones which form during interdiffusion in the range of

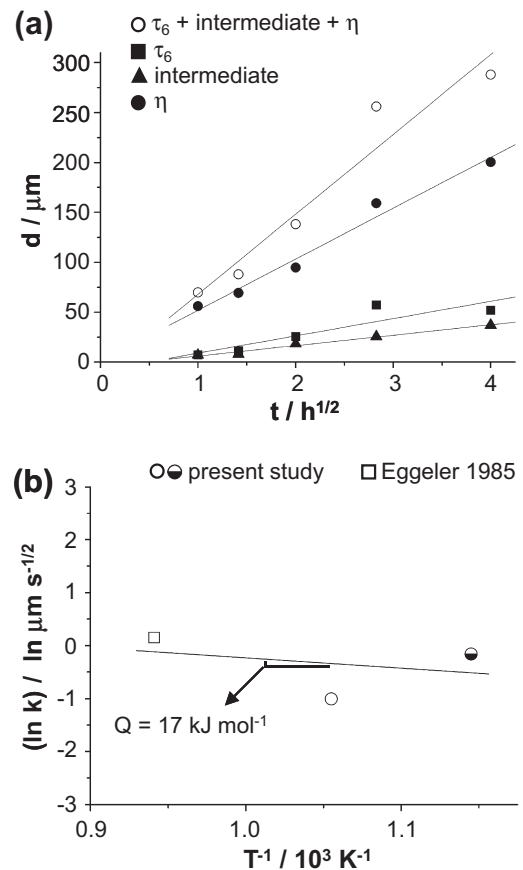


Fig. 12. Growth of the reaction layer during the reaction of steel with Al–Si alloys. (a) Thickness data from the present study plotted as a function of square root of reaction time at 600 °C. (b) Arrhenius plot of rate constants for the  $\eta$  phase from the present study and from the literature [24].

600–675 °C between a low-carbon steel (0.08 wt.% C, European grade DC04) with Al of 99.99% purity and with an Al–5 wt.% Si alloy. Investigations were performed

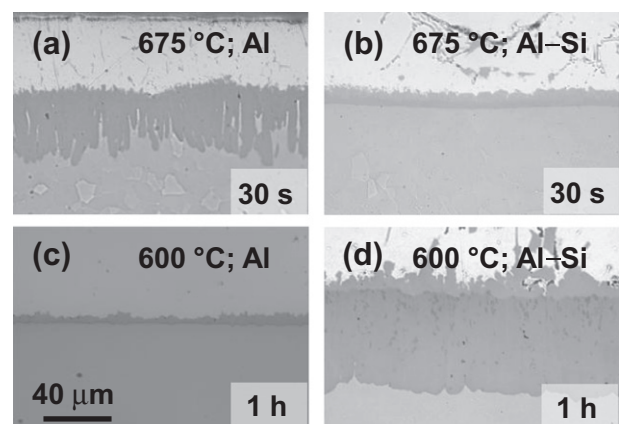


Fig. 13. Optical micrographs of reaction layers from four different interdiffusion experiments, exemplifying the inverse effect of Si on reaction layer thickness: (a) solid/liquid interaction with Al99.99 (30 s, 675 °C); (b) solid/liquid interaction with Al–5 wt.% Si (675 °C, 30 s); (c) solid/solid interaction with Al99.99 (600 °C, 1 h); (d) solid/semi-solid interaction with Al–5 wt.% Si (600 °C, 1 h).



under conditions where both materials are in the solid state, the steel is solid and the Al alloy is liquid, and, in the case of the Al–Si alloy, when the steel is solid and the Al alloy is in a semi-solid state given by a temperature within a two-phase field “mushy zone”. From the obtained results the following conclusions can be drawn:

- (1) New insights into the microstructure and evolution of reaction layers can be obtained by applying advanced characterization techniques such as EBSD and site-specific TEM specimen preparation using FIB.
- (2) In both solid/solid and solid/liquid interdiffusion experiments with low-carbon steel and Al, the  $\eta$  phase is the major constituent of the reaction layer. EBSD and TEM investigations elucidate subtle differences between those two cases: a thin  $\theta$  phase layer is present between the  $\eta$  phase and Al in case of the solid/liquid interdiffusion experiment, but cannot be detected during solid/solid interdiffusion. Thin bands of  $\beta'$  and  $\kappa$  are observed between  $\eta$  and steel in the case of solid/solid interdiffusion, but are absent after the reaction with liquid Al.
- (3) The growth of the reaction layers can be described by parabolic rate laws. Combining the rate constants from the present work and previous studies in the range of 600–800 °C, an activation energy of 190 kJ mol<sup>−1</sup> can be obtained for interdiffusion with pure Al from an Arrhenius plot. Both solid/solid and solid/liquid interdiffusion experiments can be rationalized by the same phenomenological kinetic equations.
- (4) The present results confirm previous findings that adding Si to Al melts results in a reduced growth rate of the reaction layer in a solid/liquid interdiffusion process as compared to Al melts. The outer part of the reaction layer is shown to consist of the  $\tau_5$  phase, which was previously not reported, and it is shown that the  $\tau_5$  and  $\theta$  phases constitute a significant fraction of the reaction zone, which is often assumed to consist predominantly of the  $\eta$  phase.
- (5) New results are presented showing that when low-carbon steel reacts with Al–5 wt.% Si at 600 °C, much thicker reaction layers form than when it reacts with pure Al at the same temperature. The microstructure of the reaction layer in this case is also more complex than the respective layers formed between steel and pure Al. The  $\eta$  phase again takes up the largest fraction in case of interdiffusion with Al–5 wt.% Si at 600 °C. The Si content of the  $\eta$  phase, however, is about the same as in solid/liquid reactions with Al–Si melts at 675 °C (1–2 at.%), where a growth deceleration is observed. This challenges the view that the effect of Si on inhibiting reaction layer growth can simply be attributed to Si atoms occupying structural vacancies on the  $c$ -axis of the  $\eta$  phase. Since  $\eta$  phase growth is well described by a parabolic rate equation, it is unlikely that interface reactions are responsible

for this inverse effect on reaction layer thickness. From the rate constants for interdiffusion with Al–Si alloys obtained in the present work and from previous studies, an activation energy of 17 kJ mol<sup>−1</sup> can be obtained for growth of the  $\eta$  phase. The activation energies and rate constants obtained in the present work are consistent with the observation of a faster growth rate of the reaction layer at lower temperatures in the Si-containing Al alloy relative to the case of pure Al.

## Acknowledgements

H. Springer wishes to thank Dr. Leonardo Agudo Jàcome for valuable discussions in early stages of this work. Financial support from the Max-Planck-Gesellschaft through the Max-Planck-Fellow Group for High Temperature Materials is acknowledged.

## References

- [1] Ashby MF. Materials selection in mechanical design. Burlington, MA: Butterworth-Heinemann; 2005.
- [2] Honeycombe RWK. Steels—microstructure and properties. London: Arnold; 1981.
- [3] Leslie WC, Hornbogen E. In: Cahn RW, Haasen P, editors. Physical metallurgy. Amsterdam: Elsevier; 1996.
- [4] Polmear IJ. Metallurgy of the light metals. London: Arnold; 1996.
- [5] Altenpohl D. Aluminium viewed from within. Düsseldorf: Aluminium-Verlag; 1982.
- [6] Ryabov VR. Welding of aluminium alloys to steels. Amsterdam: OPA; 1998.
- [7] Radschheit CR. Ph.D. Thesis, Universität Bremen; 1996.
- [8] Roulin M, Luster J, Karadeniz G, Mortensen A. Weld J 1999;151 [Research Supplement].
- [9] Hartwig H. Aluminium 1981;57:615.
- [10] Mechsner K, Klock H. Aluminium 1983;59:850.
- [11] Kattner UR. In: Binary alloy phase diagrams. Materials Park, OH: ASM International; 1990. p. 147.
- [12] Kubaschewski O. Iron—binary phase diagrams. Berlin: Springer Verlag; 1982.
- [13] Gosh G. In: Ternary alloys, vol. 5. Weinheim: VCH Verlagsgesellschaft; 1992. p. 394.
- [14] Krendelsberger N, Weitzer F, Schuster JC. Metall Mater Trans A 2007;38:1631.
- [15] Kidson GV. J Nucl Mater 1961;3:21.
- [16] Achar DRG, Ruge J, Sundaresan S. Aluminium 1980;56:220.
- [17] Yilmaz M, Cöl M, Acet M. Mater Charact 2003;49:421.
- [18] Heumann T, Dittrich S. Z Metall 1959;50:617.
- [19] Eggeler G. Ph.D. Thesis. Friedrich Alexander Universität, Erlangen; 1985.
- [20] Bouche K, Barbier F, Coulet A. Mater Sci Eng A 1998;249:167.
- [21] Bouayad A, Gerometta C, Belkebir A, Ambari A. Mater Sci Eng A 2003;363:53.
- [22] Eggeler G, Vogel H, Freidrich J, Kaesche H. Prak Metallogr – Pr M 1985;22:163.
- [23] Gebhardt E, Obrowski W. Z Metall 1953;44:154.
- [24] Eggeler G, Auer W, Kaesche H. J Mater Sci 1986;21:3348.
- [25] An J, Liu YB, Zhang MZ, Yang B. J Mater Process Technol 2002;120:30.
- [26] Knauscher A. Neue Hütte 1974;19:398.
- [27] Sunderasan S. Mater Forum 1993;17:301.

- [28] Kobayashi A, Machida M, Hukaya S, Suzuki M. *JSME Int J, Ser A* 2003;46:452.
- [29] Naoi D, Kajihara M. *Mater Sci Eng A* 2007;459:375.
- [30] Kurakin AK. *Phys Met Metallogr* 1970;30:108.
- [31] Smigelkas AD, Kirkendall EO. *Trans AIME* 1947;171:130.
- [32] Nicholls JE. *Corr Tech* 1964;11:16.
- [33] Denner SG, Jones RD, Thomas RJ. *J Iron Steel Inst* 1975;48:241.
- [34] Komatsu N, Nakamura M, Fujita H. *J Jpn Inst Light Met* 1968;18:467.
- [35] Agudo L, Eyidi D, Schmaranzer CH, Arenholz E, Jank N, Bruckner J, et al. *J Mater Sci* 2007;42:4205.
- [36] Modigell M, Koke J. *Mech Time-Depend Mater* 1999;3:15.
- [37] Yang YS, Tsao CYA. *J Mater Sci* 1997;32:2087.
- [38] Murray JL, McAllister AJ. *Bull Alloy Phase Diagr* 1984;5:74.
- [39] Schwartz AJ, Kumar M, Adams BL, editors. *Electron backscatter diffraction in materials science*. New York: Kluwer Academic; 2000.
- [40] Williams DB, Carter CB. *Transmission electron microscopy: a textbook for materials science*. New York: Plenum Press; 1996.
- [41] Browning ND, Chisolm MF, Pennycook SJ. *Nature* 1993;366:143.
- [42] Xiao H, Baker I. *Acta Metall Mater* 1995;43:391.
- [43] Palatnik LS, Tananko IA, Bobro YG. *Kristallografiya* 1964;9:209.
- [44] Ellner M, Mayer J. *Scripta Metall Mater* 1992;26:501.
- [45] Eggeler G, Auer W, Kaesche H. *Z Metall* 1986;77:239.
- [46] Black PJ. *Acta Crystallogr* 1955;8:43.
- [47] Yanson TI, Manyako MB, Bodak OI, German NV, Zarechnyuk OS, Cerny R, et al. *Acta Crystallogr C* 1996;52:2964.
- [48] Munson D. *J Inst Met* 1967;95:217.
- [49] German NV, Zavodnik VE, Yanson TI, Zarechnyuk OS. *Sov Crystallogr* 1989;34:439.
- [50] Corby RN, Black PJ. *Acta Crystallogr B* 1977;33:3468.
- [51] Hansen V, Hauback B, Sundberg M, Romming C, Gjønnes J. *Acta Crystallogr B* 1998;54:351.
- [52] German NV, Belskii VK, Yanson TI, Zarechnyuk OS. *Kristallografiya* 1989;34:735.
- [53] Langenscheidt G, Klein G. *Prak Metallogr – Pr M* 1977;14:251.
- [54] Shibata K, Morozumi S, Kosa S. *J Jpn Inst Met* 1966;30:382.